Check for updates

Harvesting Multidirectional Breeze Energy and Self-Powered Intelligent Fire Detection Systems Based on Triboelectric Nanogenerator and Fluid-Dynamic Modeling

Xuemei Zhang, Jie Hu, Qianxi Yang, Hongmei Yang, Huake Yang, Qianying Li, Xiaochuan Li, Chenguo Hu, Yi Xi,* and Zhong Lin Wang*

Fire warning and monitoring are very important for public safety and environmental protection. However, most of the proposed wind energy conversion devices based on triboelectric nanogenerator (TENG) only work for unidirectional and high-speed wind and face the challenge of fatigue damage and even failure caused by cyclic stress. Moreover, TENG guided by the theory of fluid dynamics needs further exploration. Herein, a flow-induced vibration effect based TENG (F-TENG) for continuously capturing and monitoring multidirectional breeze (1.8–4.3 m s^{-1}) is developed to build a self-powered intelligent fire detection system (SIFDS). A dynamic model is proposed to study the intrinsic interaction between the electrical properties of F-TENG and wind. Since the model optimized F-TENG is more adaptable to wind characteristics, it delivers better performance and higher durability compared with previous studies. Relying on the dynamic model and combining the relationship between F-TENG's electrical output and wind characteristics, a self-powered visual wind sensing system is obtained. F-TENG successfully drives some electronic devices to monitor environmental information, which is expected to provide data for SIFDS to reduce fire hazards. This study can provide an in-depth understanding of the electromechanical conversion mechanism and large-scale capture and utilization of breeze energy.

X. Zhang, J. Hu, Q. Yang, H. Yang, H. Yang, Q. Li, X. Li, C. Hu, Y. Xi
Chongqing Key Laboratory of Soft Condensed Matter Physics
and Smart Materials
Department of Automotive Engineering
State Key Laboratory of Power Transmission Equipment
and System Security and New Technology
Chongqing University Shapingba
Chongqing 400044, China
E-mail: yxi6@cqu.edu.cn
Z. L. Wang
Beijing Institute of Nanoenergy and Nanosystems
Chinese Academy of Sciences
Beijing 100083, China
E-mail: zhong.wang@mse.gatech.edu
Z. L. Wang
Georgia Institute of Technology
Atlanta, GA 30332, USA

1. Introduction

Fire accident is one of the major disasters that threaten the public safety of lives and assets, and environmental protection.[1] The World Fire Statistics 2019 reveals that from 1993 to 2017, an average of 3.8 million fires occurred each year, killing 1 million people at least.[2] Many fire cases manifest that fire risk prediction, fire alarm, and rescue in time are of great significance to reduce damages. Intelligent fire detection systems can be used to predict the fire risk, give early warning to the fire, and provide guidance to fire rescue.[3] While during fire accidents, most of the remote rescue electronic equipment stop working because of power failure.[4,5] Therefore, self-powered intelligent fire detection systems (SIFDS) are urgently needed.

The newly invented triboelectric nanogenerator (TENG) as a mechanical energy collection device was proposed by Wang's group in 2012.[6] It can be used to capture wind energy from the environment to solve the energy supply and sensing issues during a fire.[7] Compared with traditional turbines with large volume and low space utilization,[8] TENG has the characteristics of small size,[9] low cost,[10] and good response to low-frequency mechanical vibration.[11] It can be employed to scavenge the wind energy in the low-speed region, further optimize the utilization of space, and generate electricity near the ground, which can not only complement the traditional power supply such as batteries and power plants, but also reduce the thousands of feet of wiring required by wind turbines and power plants.[12] The previous TENG based on fluid-induced vibration (FIV) operated continuously depending on the interaction between wind and elastomer.[13–15] However, the elastomer is subjected to complex stress and persistent fatigue rupture during working, which significantly affects the life and output performance of the device.[16,17] Generally, natural wind flows in a random direction and at low speed near the earth's surface.[18] Therefore, the design of low starting wind speed and multidirectional wind energy collection device is another current requirement for the FIV based TENG.[19,20] Since the wind energy harvesters involve the coupling of fluid dynamics, solid mechanics, electrical

**ADVANCED
SCIENCE NEWS**

www.advancedsciencenews.com

**ADVANCED
FUNCTIONAL
MATERIALS**

www.afm-journal.de

circuits, and electronic devices, the flow mechanism, and the principles of mechanical energy and electrical energy conversion under complex conditions need to be further studied.

Herein, a TENG based on FIV (named as F-TENG) is illustrated to enduringly acquire and monitor breeze energy in an arbitrary direction. The F-TENG contains six identically TENG units and rotatable triggers with a labor-saving lever structure. This special structure not only replaces the elastomer in the traditional FIV based TENG with the rotatable trigger, overcomes the fatigue damage caused by deformation, reduces the F-TENG's starting wind speed, but also allows it to collect wind energy in multiple directions. First, based on the theory of fluid mechanics and the contact-separation mode of TENG, a dynamic model (wind-impact object model) of mechanical energy and electrical energy conversion was proposed to explore the intrinsic interaction between the electrical performance of the device and wind. Subsequently, based on the dynamic model of this device, the influences of various structural parameters on the output performance of the F-TENG were explored from theory and experiment in depth. After the structural design and optimization on model and experiment, F-TENG can effectively convert tiny mechanical energy from the wind (1.8–4.3 m s^{-1}) in random directions into electrical, and monitor the wind by self-powered for a super long time. Based on these environmental monitors, the basic data can be provided for SIFDS to reduce the threat of fire to public safety and social development. This work can provide a direction for the in-depth understanding of the fluid-structure interaction mechanism, serve the purpose of capturing wind power as clean energy in the Internet of Things (IoT) era, and provide a practical solution for taming the problems caused by fire as well.

2. Results and Discussion

2.1. Structure and Working Principle

SIFDS is vital to maintain the security of public. Abundant miniaturized and distributed sensors are needed in the IoT era. Here F-TENG network not only effectively converts wind energy into electricity and supplies power for electrical devices, as a supplement to traditional energy, but also acts as self-powered wind direction and speed sensors. In this way, environmental information including the acquisition of fire location and other fire rescue information can be monitored with the SIFDS. These prospective applications are proposed in **Figure 1**a. A rotatable trigger contains the arc part and inclined plate part, the unfolded plan view and 3D schematic of the rotatable trigger are displayed in Figure S1a,b, Supporting Information. Due to the symmetrical distribution and the lever structure of the rotatable trigger, periodic rotations about a fixed axis can be achieved under fluid–solid interaction, that is, FIV.[12a,21] Figure S1c, Supporting Information illustrates the particular motion state of the rotatable trigger. An intact vibration period occurs when the trigger rotates periodically between critical position state I and state II.

To further validate the vibration mechanism, the velocity contour (Figure 1b) is also simulated based on the fluid–solid bidirectional coupling platform of ANSYS software, when the rotatable trigger is exposed to wind in 4.3 m s^{-1}. The structure of F-TENG is visualized in Figure 1c, which includes a panorama (I), a cross section view (II), and a top view of the F-TENG (III), and the corresponding photos of the as-fabricated F-TENG device are presented in Figure 1d(I–III). The F-TENG consists of six independent TENG units, six rotatable triggers, a 3D-printed six frustums of a pyramid used as a frame, and six pairs of magnets with the same poles. The manufacturing process and the 3D drawings of the TENG unit are shown in Figure S2a,b, Supporting Information, respectively. Here the repulsive force of the magnet is used to overcome the electrostatic adsorption force produced during the operation of the F-TENG.

Because the six F-TENG units own the same structure, one single F-TENG unit is used to illustrate the mechanism of power generation. The aluminum (Al) foil connected to the rotatable trigger is called electrode A acting as both electrode and friction layer, and the other Al foil bonded to the frustum of a pyramid is called electrode B. In addition, the polytetrafluoroethylene (PTFE) film is attached with electrode B and plays the role of another friction material. When F-TENG is placed in the continuous wind, periodically rotating about a fixed axis and contacting with the frustum of a pyramid occur in the rotatable trigger. So the electrode A and PTFE in the F-TENG unit periodically contact and separate. Based on the combined action of electrification and electrostatic induction, the detailed charge generation and transfer process of F-TENG with contact and separation mode are schematically illustrated in Figure 1e. In the beginning, electrode A contacts with PTFE film (Figure 1e, state I), due to the stronger ability of PTFE to attract negative charges, a certain amount of negative charges occur in the surface of PTFE, and the same number of positive charges appear in electrode A. Under the effect of wind, the rotatable trigger rotates to a certain angle with the frustum of a pyramid, and electrode A separates with PTFE film (Figure 1e, state II). According to the electrostatic induction, free electrons on electrode B transfer to electrode A through the external load to balance the potential difference. Therefore, a pulse electric current is generated from electrode A to electrode B. There follows an extreme position (Figure 1e, state III), that the rotatable trigger keeps rotating in the same direction, and the angular velocity slows down to zero as well. Subsequently, the applied torque can be produced by all the external forces, which can cause the rotatable trigger of the lever structure to rotate in reverse (Figure 1e, state IV). The two friction materials get close to each other, and electrons flow backward through the external load. Finally, electrode A contacts with PTFE film again, and TENG returns to the original state I. Continuous alternating current is generated in the external circuit, based on this periodic oscillating motion.[22] The actual photograph of a single unit is shown in Figure 1e (V). This F-TENG shows great potential in breeze energy harvesting with higher energy conversion and lower starting wind speed compared with the previous works,[13,14,16–18,20,23–28] illustrated as Figure 1f, which provides a feasible scheme for the earth's surface wind energy collection.

2.2. Dynamic Model of F-TENG from Wind Force

When the wind flowing at a certain rate impinges on a trigger, the wind slows down vertically near the impact surface, deflects and accelerates in the radial direction, leading to wind flows
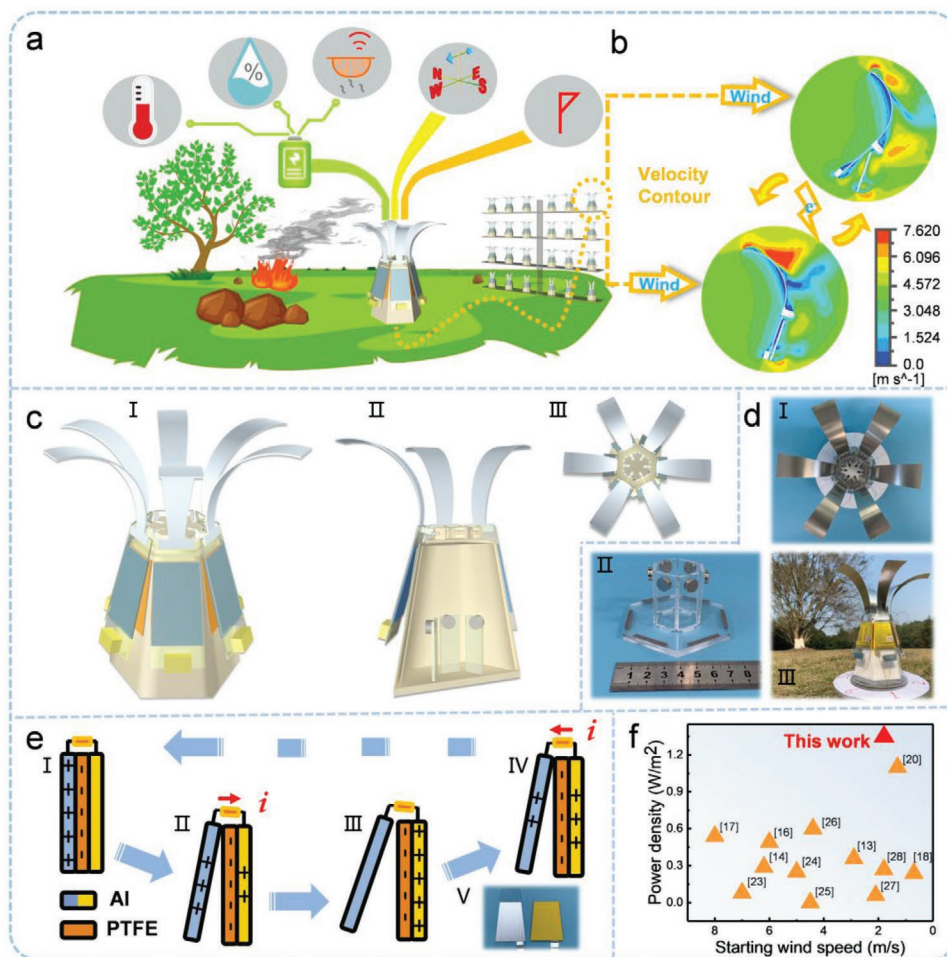
Figure 1. Application scenario and operating principle of the F-TENG. a) Prospect of the F-TENG for self-powered intelligent fire protection systems applications. b) Simulations of velocity contour for a single rotatable part at the wind speed 4.3 m s⁻¹. c) Schematic diagram of the F-TENG: I) panorama, II) cross section view, and III) top view. d) Image of the as-fabricated F-TENG device: I) top view, II) magnet installation drawing inside the frustum of a pyramid, and III) panorama. e) Operating principle I–IV) and photograph V) of the TENG unit. f) Comparison of the output power densities and starting wind speeds reported works based on flow-induced vibration.
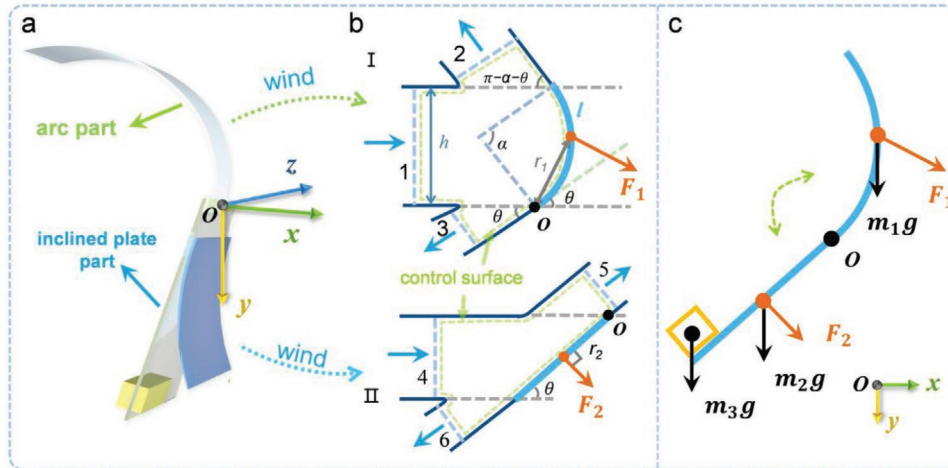
radially outward at the surface.[29] The impinging region, because of this flow characteristic, is also called the flow deflection zone, in which the wind can produce a strong impact on the trigger.[30] Thus we call the process of wind interacting with a rotatable trigger as the wind-impact object model. For the rotatable trigger (**Figure 2**a), the shape and force of the upper and lower parts are different, so the studies of the upper arc part and the lower inclined plate part are carried out, respectively. Here, the origin point O of the xyz coordinate system that satisfies the right-hand rule is selected at the center of the fixed axis for rotation. Moreover, the control volume approach is selected to study the flow deflection zone. Figure 2b(I,II) shows the suitable control volume, surrounded by the control surface with the dashed green line, the arc part and the inclined plate part when the wind blows. When the wind impacts the rotatable trigger, the impact forces $\overline{F_1}$ and $\overline{F_2}$ will be generated on the arc part and the inclined plate part respectively.[31] Note that some regions of the surface correspond to physical boundaries (the walls of the trigger) and others (at sections 1–6) are parts of the imaginary surface (inlets or outlets). The basic parameters

of the two parts are marked in the lateral view of Figure 2b(I,II) and the unfolded plan view of Figure S1a, Supporting Information. Figure S1a, Supporting Information depicts that both the arc part and the inclined plate part of the trigger are symmetrically distributed about the plane formed by z and y axis.

In the wind-impact object model, first, it is necessary to determine the force exerted on the object by the wind assumed to be a continuous incompressible fluid without friction. The equations of Bernoulli, continuity, and momentum can all be applied to the situation. Apply the Bernoulli equation in the control volume to evaluate the flow rate of each outlet.

$$gz + \frac{P}{\rho} + \frac{v^2}{2} = \text{constant} \tag{1}$$

where g is the acceleration of gravity, z is the height of any point in the control volume from the xoz plane, P and v are the average pressure and the velocity of wind at any point, respectively. ρ is the density of the air. In there, the air is very light, so the acceleration of gravity is ignored. Atmospheric pressure

ADVANCED
SCIENCE NEWS
www.advancedsciencenews.com

ADVANCED
FUNCTIONAL
MATERIALS
www.afm-journal.de

Figure 2. The wind-impact object model. a) 3D schematic of the rotatable trigger. b) Schematic model of wind impinging on the arc part I and the inclined plate part II. c) Force analysis diagram of the rotatable trigger under the combined action of wind field and gravity field. *xyz* coordinate system satisfies the right-hand rule.

acts on sections 1–6 of the control volume, so the pressure in all inlets and outlets are equal to the atmospheric pressure, and the magnitude of flow rate at each section is the same.

$$v = v_1 = v_2 = v_3 = v_4 = v_5 = v_6 \tag{2}$$

where v is a constant, v_1–v_6 are average speeds of wind at sections 1–6 in Figure 2b, respectively.

Then, the arc part and the inclined plate part are explored respectively. First, for the arc part, the volume flow rate Q (per unit time), through the control surface section with area A, is

$$Q = vA \tag{3}$$

analyze the arc part at any rotation position, referring to the geometry displayed in Figure 2b(I), so the angle between the line of the upper and lower vertices and the plane of *xoz* is $\frac{\alpha}{2} + \theta$, hence

$$Q_1 = vhd_1 = \frac{2lvd_1}{\alpha}\sin\frac{2lvd_1}{\alpha}\sin\frac{\alpha}{2}\sin\left(\frac{\alpha}{2} + \theta\right) \tag{4}$$

where Q_1 is the volume flow rate (per unit time) through section 1, h is the height of section 1 in the xoz plane, d_1 is the average width of the arc part in the z direction, and the evaluation process of d_1 is given in Supporting Information note. l and α are the arc length of the arc part and the corresponding central angle. θ is the angle between the tangent line at the rotation axis of the arc part and the x axis. Here the radius of curvature (R), arc length (l), and central angle (α) of the arc part satisfy the relationship ($R = \frac{l}{\alpha}$).

Apply the continuity equation

$$Q_1 = Q_2 + Q_3 \tag{5}$$

where Q_2 and Q_3 are the volume flow rate (per unit time) through sections 2 and 3, respectively.

Then apply the momentum equation (per unit time)

$$\sum_{\text{out}}\rho Q\vec{v}_{\text{out}} - \sum_{\text{in}}\rho Q\,\vec{v}_{\text{in}} = \sum\vec{F} \tag{6}$$

writing the x and y components of the momentum equation give

$$F_{1x} = -F'_{1x} = -\rho Q_2 v\cos(\pi - \alpha - \theta) + \rho Q_3 v\cos\theta + \rho Q_1 v \tag{7}$$

$$F_{1y} = -F'_{1y} = \rho Q_2 v\sin(\alpha + \theta) - \rho Q_3 v\sin\theta \tag{8}$$

F'_{1x} and F'_{1y} are the magnitudes of external force components from the arc part acting on the control volume, F_{1x} and F_{1y} are the magnitudes of impact force components from the control volume acting on the arc part. Newton's third law states that for each force, there is an equal and opposite reaction force, so this force, F'_{2x}, will be the same as F_{1x}, except in the opposite direction.[32] Hence, F_y and F'_{1y} should satisfy the same relationships.

$$\vec{F}_1 = F_{1x}\vec{i} + F_{1y}\vec{j} \tag{9}$$

where $\vec{i}$ and $\vec{j}$ are the unit vectors in the x and y directions. From the effect of F_{1x} and F_{1y}, the resultant force ($\overline{F}_1$) of the two only makes the arc part rotate around the center of rotation, without the effect of squeezing or stretching inward. Therefore, the component of $\overline{F}_1$ is equal to zero in the tangential direction of the center of gravity,

$$F_{1x}\cos\left(\frac{\alpha}{2} + \theta\right) - F_{1y}\sin\left(\frac{\pi}{2} + \theta\right) = 0 \tag{10}$$

Using these results in Equations (5), (7), (8), and (10) give

$$Q_2 = \frac{Q_1}{2}\left[1 - \frac{\cos\left(\frac{\alpha}{2} + \theta\right)}{\cos\left(\frac{\alpha}{2}\right)}\right] \tag{11}$$

ADVANCED
SCIENCE NEWS
www.advancedsciencenews.com

ADVANCED
FUNCTIONAL
MATERIALS
www.afm-journal.de

$$Q_3 = \frac{Q_1}{2}\left[1 + \frac{\cos\left(\frac{\alpha}{2}+\theta\right)}{\cos\left(\frac{\alpha}{2}\right)}\right] \quad (12)$$

According to geometric relation, the magnitude of moment arm of $\vec{F_1}$ is obtained

$$r_1 = 2\frac{l}{\alpha}\sin\frac{\alpha l_1}{2l} \quad (13)$$

The calculation of l_1 is shown in Supporting Information note.

So that, the torque generated by $\vec{F_1}$ and the gravity of the arc part gives

$$\overrightarrow{M_1} = \vec{r_1} \times \vec{F_1} + \overrightarrow{M_{G1}} \quad (14)$$

where $\overrightarrow{M_{G1}}$ is the torque generated by the gravity of the arc part (m_1). Substituting yields, the magnitude of $\overrightarrow{M_1}$ is

$$M_1 = 2\rho R^2 v^2 d_1 \sin\frac{\alpha}{2}\sin\left(\frac{l_1}{2R}\right)\sin\left(\frac{\alpha}{2}+\theta\right)\left\{\sin\left(\frac{l_1}{2R}+\theta\right)\left[2 - \frac{\cos\theta\cos\left(\frac{\alpha}{2}+\theta\right)}{\cos\frac{\alpha}{2}} - \frac{\cos(\alpha+\theta)\cos\left(\frac{\alpha}{2}+\theta\right)}{\cos\frac{\alpha}{2}} + \cos\theta - \cos(\alpha+\theta)\right]\right.$$
$$\left. + \cos\left(\frac{l_1}{2R}+\theta\right)\left[\sin(\alpha+\theta) + \frac{\cos\left(\frac{\alpha}{2}+\theta\right)\sin(\alpha+\theta)}{\cos\frac{\alpha}{2}} - \sin\theta + \frac{\sin\theta\cos\left(\frac{\alpha}{2}+\theta\right)}{\cos\frac{\alpha}{2}}\right]\right\} + 2R\sin\left(\frac{l_1}{2R}\right)\cos\left(\frac{l_1}{2R}+\theta\right)m_1\,g \quad (15)$$

the direction of $\overrightarrow{M_1}$ is along the positive direction of the z axis (perpendicular to paper inward).

In addition, for the inclined plate part (Figure 2b(II)), using the result in Equation (3), we obtain

$$Q_4 = \frac{(w_4 + w_5)vl_4\sin\theta}{2} \quad (16)$$

where Q_4 is the volume flow rate (per unit time) through section 4, the plan of the inclined plate is a trapezoid, l_4 is the height of the trapezoid. w_4 and w_5 are the widths of the top and bottom of the trapezoid, respectively.

Apply the continuity equation

$$Q_4 = Q_5 + Q_6 \quad (17)$$

where Q_5 and Q_6 are the volume flow rate (per unit time) through sections 5 and 6, respectively.

According to the momentum equation of Equation (6), writing the x and y components of the momentum equation give

$$F_{2x} = -F'_{2x} = \rho Q_6 v\cos\theta - \rho Q_5 v\cos\theta + \rho Q_4 v \quad (18)$$

$$F_{2y} = -F'_{2y} = \rho Q_6 v\sin\theta - \rho Q_5 v\sin\theta \quad (19)$$

F'_{2x} and F'_{2y} are the magnitudes of external force components from the inclined plate part acting on the control volume, F_{2x} and F_{2y} are the magnitudes of impact force components from

the control volume acting on the inclined plate part. According to Newton's third law, this force, F'_{2x}, is the same as F_{2x}, except in the opposite direction. So F'_{2y} and F_{2y} satisfy the same relationships.

$$\overrightarrow{F_2} = F_{2x}\vec{i} + F_{2y}\vec{j} \quad (20)$$

From the effect of the resultant force ($\overrightarrow{F_2}$) of F_{2x} and F_{2y}, which only makes the inclined plate part rotate around the center of rotation. Therefore, the component of $\overrightarrow{F_2}$ is equal to zero in the direction parallel to the inclined plate, thus

$$F_{2x}\cos\theta + F_{2y}\sin\theta = \rho Q_6 v - \rho Q_5 v + \rho Q_4 v\cos\theta = 0 \quad (21)$$

Using these results in Equations (17)–(21) give

$$Q_5 = \frac{Q_4}{2}(1+\cos\theta) \quad (22)$$

$$Q_6 = \frac{Q_4}{2}(1-\cos\theta) \quad (23)$$

$$F_2 = F_{2x}\sin\theta + F_{2y}\cos\theta = \rho Q_4 v\sin\theta \quad (24)$$
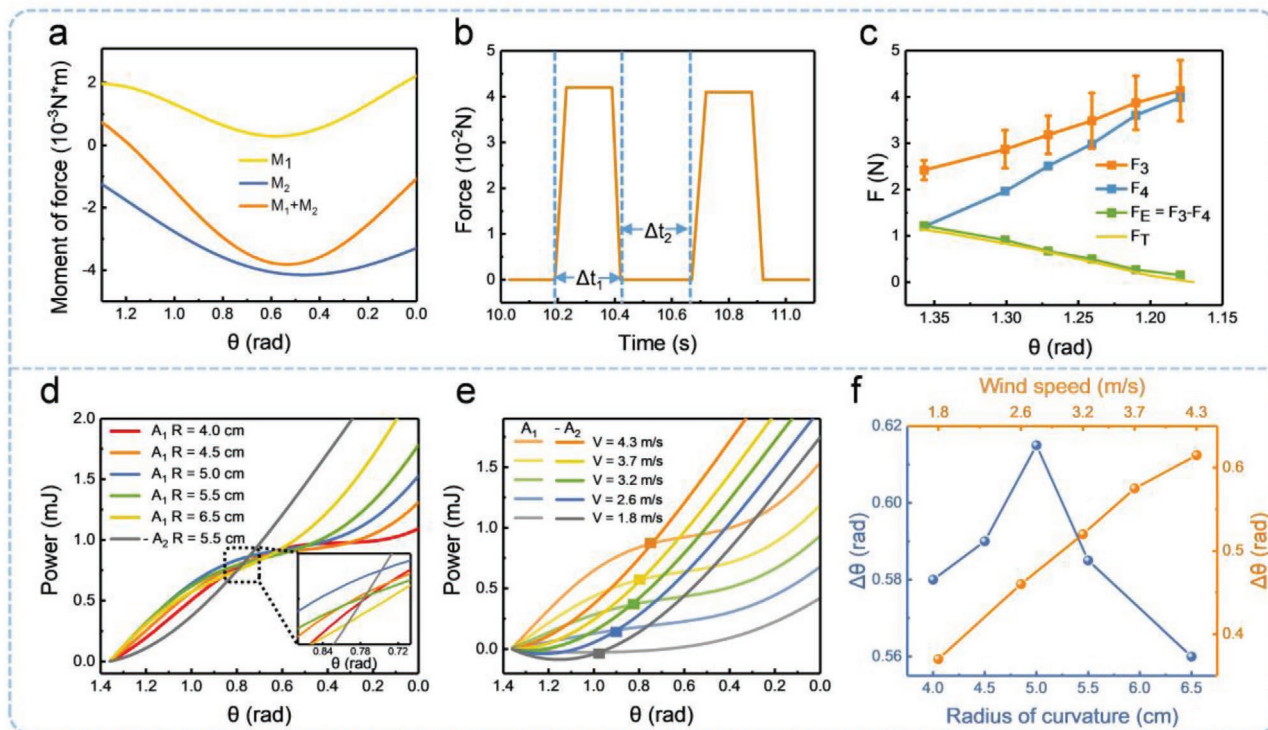
so that, the total torque of the inclined plate part is

$$\overrightarrow{M_2} = \vec{r_2} \times \overrightarrow{F_2} + \overrightarrow{M_{G2}} + \overrightarrow{M_{G3}} + \overrightarrow{M_B} + \overrightarrow{M_e} \quad (25)$$

where $\vec{r_2} \times \overrightarrow{F_2}$ is the torque generated by F_2, $\overrightarrow{M_{G2}}$ is the torque generated by the gravity of the inclined plate part (m_2g), $\overrightarrow{M_{G3}}$ is the torque generated by the extra weight added to the edge of the inclined plate, the total mass (m_3) of extra weight includes the weight of Al-nickel alloy block for weight adjustment and the magnet. $\overrightarrow{M_B}$ is the torque generated by the repulsive force generated by the inner and outer magnets, and $\overrightarrow{M_e}$ is the torque generated by the electrostatic adsorption on internal and external friction layers. In the experiment, the magnet pairs are added to overcome electrostatic adsorption, thus the sum of $\overrightarrow{M_B}$ and $\overrightarrow{M_e}$ is equal to zero.

Substituting known values, the magnitude of torques $\overrightarrow{M_2}$ can be obtained

$$M_2 = \rho Q_4 v r_2\sin\theta + m_2 g r_2\cos\theta + m_3 g l_4\cos\theta$$
$$+ \frac{(w_4+w_5)\rho v^2 l_4 r_2\sin\theta}{2} + m_2 g r_2\cos\theta + m_3 g l_4\cos\theta \quad (26)$$

the direction of $\overrightarrow{M_2}$ is along the negative direction of the z axis (perpendicular to paper outward). The evaluation process of the magnitude of moment arm (r_2) of $\overrightarrow{F_2}$ is presented in Supporting Information note.

ADVANCED
SCIENCE NEWS
www.advancedsciencenews.com

ADVANCED
FUNCTIONAL
MATERIALS
www.afm-journal.de

Figure 3. Theoretical calculations from the wind-impact object model. a) The torque versus angle θ for the arc part (M_1), the inclined plate part (M_2) and the rotatable trigger ($M_1 + M_2$). b) The enlarged force curve of the edge of the inclined plate squeezing the dynamometer at the position of $\theta = 1.8$ rad. c) Extrusion force (F_3), impact force (F_4), and the experimental force ($F_E = F_3 - F_4$) and theoretical force generated by the combined torque, at the edge of the inclined plate. d) Relationship between the work done by M_1 (A_1), the work done by M_2 (A_2), and angle θ, under the different radius of curvature (R) of the arc part. e) Influence on A_1 and A_2 caused by the varying of wind speed (with R fixed at 5 cm). f) The maximum angle of rotating for the rotatable object ($\Delta\theta$) versus R, and $\Delta\theta$ versus wind speed.

Under the effect of all the force, the object rotates back and forth about the point of O, along the direction of the arrow, which is shown in Figure 2c. The calculation results of the wind-impact object model are shown in **Figure 3**a. The angle θ gradually decreases, and both the magnitude of torques M_1 and M_2 show a trend of decreasing first and then increasing. Moreover, when θ is large, the sum of M_1 and M_2 ($M_1 + M_2$) is greater than zero, and when θ is small, it is less than zero, which follows the universal law. Only when $M_1 + M_2$ is greater than zero at first, and then gradually less than zero, will the angular velocity (ω) of rotation accelerate from zero first, subsequently, slow down to zero gradually, and then the object rotates in the opposite direction. The rotation progress is in Figure S1c, Supporting Information state I to state II.

To verify the wind-impact object model, the theoretical force ($F_T = \dfrac{M_1 + M_2}{l_4}$) and the experimental force (F_E) generated by the sum of M_1 and M_2 on the edge of the inclined plate are used for comparison. The theoretical force (F_T) is directly calculated using the relationship between the above torque and force. In the experiment, since the experimental force (F_E) cannot be measured directly, it can be obtained by subtracting the extrusion force (F_3) on the edge of the inclined plate on the dynamometer from the impact force (F_4) due to rotation at any angle θ, thus $F_E = F_3 - F_4$. The test result of the extrusion force (F_3) measured by the dynamometer is displayed in Figure S3,

Supporting Information in the condition that $\theta = 1.8$ rad, and the corresponding enlarged version is presented in Figure 3b.

Apply the theorem of momentum, considering the scalar form

$$I = F_4 \Delta t_1 = m \Delta v = m l_4 \Delta \omega \tag{27}$$

where I is the impulse, Δt_1 is the duration of the impact process, m is the total mass of the object, and $\Delta\omega$ is the change angular velocity of the object before and after impact.

Thus the impact force can be known when the angular velocity (ω_1) at the moment of impact is replaced by the mean angular velocity (ω_2) before impact

$$F_4 = \frac{m l_4 \Delta \omega}{\Delta t_1} = \frac{m l_4 (\omega_1 - 0)}{\Delta t_1} = \frac{m l_4 (\omega_2 - 0)}{\Delta t_1} = \frac{m l_4 (\theta_0 - \theta_2)}{\Delta t_1 \Delta t_2} \tag{28}$$

where θ_0 is the angle between the inclined plate part and the positive direction of the x axis when the initial angular velocity of the object is zero. And θ_2 is the angle when the extrusion force on the object is tested with a dynamometer at any position. Δt_2 is the time interval for the inclined plate part to hit the dynamometer twice.

As presented in Figure 3c, F_E is basically the same as F_T, except that F_E is slightly larger than F_T, which is mainly caused by replacing the angular velocity with the average angular

**ADVANCED
SCIENCE NEWS**
www.advancedsciencenews.com

**ADVANCED
FUNCTIONAL
MATERIALS**
www.afm-journal.de

velocity at the moment of hit when calculating F_4. The above results confirm the effectiveness and correctness of the wind-impact object model, so the following research is mainly based on the calculation results of the above model.

In the conductor-to-dielectric TENG, the open-circuit voltage (V_{OC}) is an important index to measure the output performance of a device, according to the following equation:[33]

$$V_{oc} = \frac{\sigma_c z(t)}{\varepsilon} \tag{29}$$

where σ_c is the saturated charge density on the surface of the dielectric, $z(t)$ is the distance between the dielectric layer and electrode, and ε is the dielectric constants of dielectric, respectively. When σ_c and ε remain constant, the V_{OC} is basically determined by the separation distance of $z(t)$. During the vibration of the rotatable trigger, $z(t)$ is proportional to the rotation angle ($\Delta\theta$)

$$z(t) \propto \Delta\theta = \theta_0 - \theta_2 \tag{30}$$

hence, if θ_2 is determined, the influence of the factors that need to be studied further on V_{OC} can be directly confirmed.

For this wind-impact object model, however, both the bending degree of the arc part and the speed of the wind will affect $z(t)$, by changing the combined torque of the arc part (M_1) and the total torque of the inclined plate part (M_2). The change in M_1 and M_2 directly affect the work done

$$A = A_1 + A_2 = \int_{\theta_0}^{\theta_2} M_1 d\theta + \int_{\theta_0}^{\theta_2} M_2 d\theta \tag{31}$$

where A_1 and A_2 are the work done by M_1 and M_2 calculated by integrating θ from θ_0 to θ_2, respectively. θ_0 and θ_2 respective are the angles between the tangent line at the rotation axis of the arc part and the xoz plane, when the trigger is in contact with the frustum of a pyramid (Figure S1c, Supporting Information, state I) and when the trigger is rotated to an arbitrary position. A is the sum of A_1 and A_2. In clockwise rotation, the torque M_2 is always doing negative work, hence $A_2 < 0$, the numerical results of the relationship between work done and the angle of θ at different radius of curvature R and different wind speeds are shown in Figure 3d,e, respectively. The wind speed is fixed to 4.3 m s^{-1} in Figure 3d, and the radius of curvature R is fixed to 5 cm in Figure 3e. To make it easier to understand the relationship between A_1 and A_2, the negative of A_2 ($-A_2$) is expressed in Figure 3d,e. Furthermore, the rotational kinetic energy (E) of the rotatable trigger can be expressed by this formula:

$$E = \frac{1}{2} J \omega^2 \tag{32}$$

here J is the moment of inertia of the rotatable trigger. When the object is in state I (Figure S1c, Supporting Information) and the TENG unit is in contact, the initial angular velocity is equal to zero $\omega_0 = 0$, and when the trigger rotates to the minimum angle of $\theta_2 = \theta_1$ (Figure S1c, Supporting Information, state II), the angular velocity is zero, as well $\omega_1 = 0$, therefore, the change

of rotational kinetic energy of the object from state I to state II can be expressed as follows:

$$\Delta E = \frac{1}{2} J\omega_1^2 - \frac{1}{2} J \omega_0^2 = 0 \tag{33}$$

The theorem of the kinetic energy of a rigid body rotating about a fixed axis shows that the work done by external forces in rotating a rigid body about a fixed axis is equal to the change in rotational kinetic energy of the body.[34] Using these results in Equation (33)

$$A = \Delta E = \int_{\theta_0}^{\theta_1} M_1 d\theta + \int_{\theta_0}^{\theta_1} M_2 d\theta = 0 \tag{34}$$

so that θ_1 corresponds to the second abscissa at the intersection of the two curves A_1 versus θ and $-A_2$ versus θ. Through the structural design and mechanical analysis, the relationship of the energy and angle (θ) has been obtained. In addition, Figure 3f displays the relationship between the rotation angle $\Delta\theta$ and radius of curvature R, as well as between the rotation angle $\Delta\theta$ and wind speed, in theoretical. Interestingly, with the increase of R, $\Delta\theta$ first increases and then decreases, while with the increase of wind speed, $\Delta\theta$ basically increases linearly.

In summary, in the wind-impact object model, the impact force of the wind can produce varying torque on the trigger, so that the rotatable trigger can rotate periodically about a fixed axis under the wind field. Theoretically, both the shape of the arc part and the wind speed will affect the amplitude of the trigger's motion and output performance of the device. Based on the above theoretical model and calculated results, the device with excellent performance has been designed, and in the next section, the output performance of the device will be explored in the real wind field and the corresponding practical application.

2.3. Structural Optimization

The foregoing analyses show that both the structure characteristics of the object and the flow characteristics of the fluid, in the wind-impact object model, will influence the work of the device and the output performance. The basic parameters of steel, such as the shape, the radius of curvature R, the thickness, and the weight of adding mass are all adjusted to obtain the best electrical output signal for a single F-TENG unit with an effective area of 10 cm^2, as demonstrated in **Figure 4** and Figure S4, Supporting Information.

Because the steel sheet has the characteristics of convenient cutting, easy forming, and durability, the steel sheet was chosen to fabricate the arc part of the rotatable trigger. Different shapes of steel sheets are subjected differently to the impact of the wind. Here, four different arc shapes of steel sheets with the same area were designed, includes upright trapezoid, bayonet shape, rectangle, and inverted trapezoid. The corresponding tiled physical photo can be seen in Figure S4a, Supporting Information. V_{OC}, short-circuit current (I_{SC}) and transferred charges (Q_{SC}) of F-TENG with the four shapes of steel sheets were measured at the wind speed of 4.3 m s^{-1}. It can be seen from Figure S4b, Supporting Information, under the same conditions, the electrical
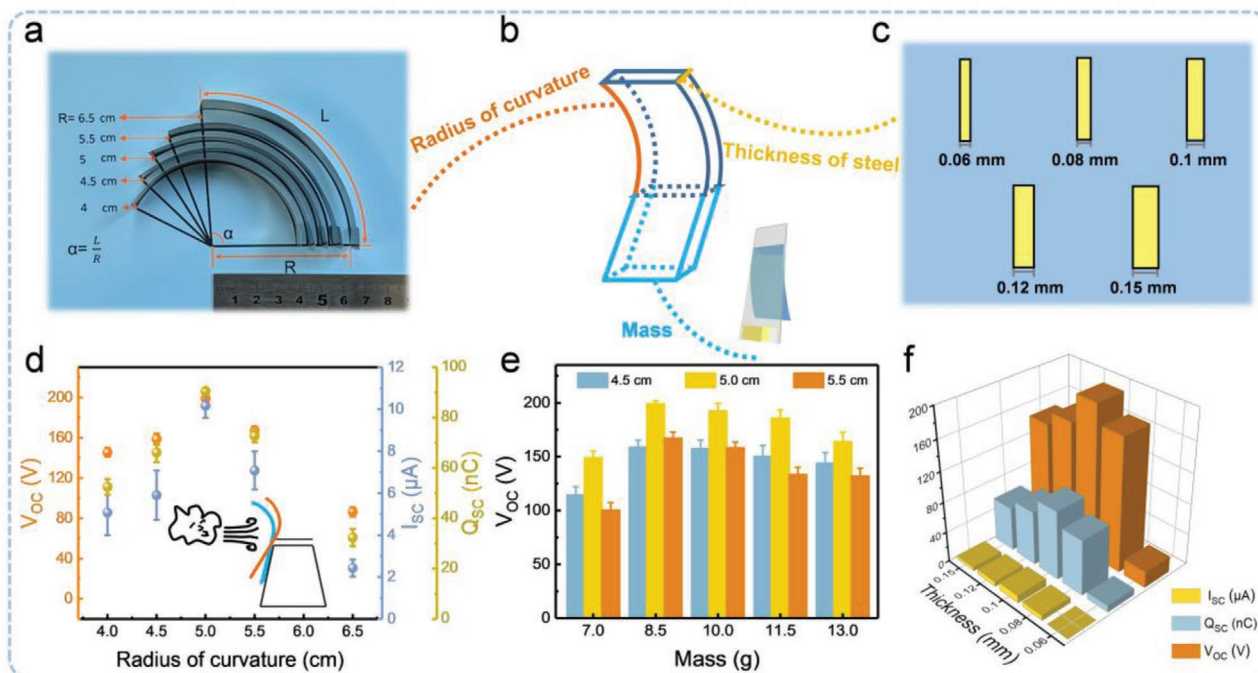
Figure 4. Structure parameters influence on the output of F-TENG (wind speed fixed at 4.3 m s^{-1}). a) Photograph of the arc steel sheets with different radius of curvature (R). b) Schematic diagram of the rotatable trigger. c) Sketches of the arc steel sheets with different thicknesses. d) Output electrical performance within arc steel sheets under various R. e) Open-circuit voltage (V_{OC}) of F-TENG while varying the mass of inclined plate part. f) Output electrical performance of F-TENG within arc steel sheets under various thicknesses.

output of F-TENG with rectangular and inverted trapezoidal steel sheets are more than twice as large as that of upright trapezoidal and bayonet shaped steel sheets, and the inverted trapezoidal steel sheet shows the best performance. This is because the biggest moment arm r_1 occurs in the inverted trapezoid. Based on this result, the inverted trapezoidal steel sheet as the arc part of the F-TENG was selected to capture wind energy.

From Equation (5), the quantitative relationship among arc length l, the radius of curvature R and center angle α can be obtained. Photographs of steel sheets with different curvatures are shown in Figure 4a. R can indicate the curve degree of the steel sheet (Figure 4b). In addition, the thickness refers to the distance between the left and right sides of the curved steel sheet, which is a parameter reflecting the toughness of the steel sheet (Figure 4c). As depicted in Figure 4d, different R from 4.0 to 6.5 cm were employed to explore the output performance of the TENG, which indicates that the optimal output performance can be obtained at $R = 5.0$ cm. The variation trend of output with R is consistent with that of the difference in the angle of rotation $\Delta\theta$ with R in Figure 3f, which proves the effectiveness of the wind-impact object model again.

The rotatable trigger can be regarded as a lever with different force arms. According to Archimedes' law of leverage, under the external force, the longer the force arm, the greater the motion range of the object. Therefore, the device can be driven under the action of a breeze. To ensure the effective periodic operation of TENG, ignoring the small influence of friction resistance, and focusing on the force caused by the gravity of the inclined plate and the extra weight added to the edge of the inclined plate. The weight of the inclined plate and the magnet are controlled unchanged, and the load on the edge of the inclined plate increases continuously. As the total weight of the inclined plate part increases from 7.0 to 13.0 g, the arc steel sheets with different curvatures show different responses. The results show that the V_{OC}, I_{SC}, and Q_{SC} of TENG increase first and then decrease no matter the steel sheet with a curvature of 4.5, 5.0, or 5.5 cm (Figure 4e). And the maximum output performances are 199 V, 10 µA, and 90 nC (5.0 cm, 8.5 g) as shown in Figure 4e and Figure S4b,c, Supporting Information, respectively.

Moreover, the toughness (determined by thickness) of the arc steel sheet affects its deformation ability when it interacts with the wind. Hence, the electrical output of TENG was studied with different thicknesses of the steel sheet from 0.06 to 0.15 mm (Figure 4f). Under the wind speed of 4.3 m s^{-1}, the most matching thickness of the steel sheet is 0.1 mm. The reason is that when the steel sheet thickness is 0.1 mm, it can not only effectively transfer the impact force of the wind to the rotatable trigger with the lever structure, but also realize the reverse rotation by slightly deformation rather than stay at the position of the maximum rotation angle. Based on the above experimental results, with optimized structure, the output performance of a single F-TENG unit can achieve the optimal value, so the single unit with the best performance is used to fabricate the F-TENG with six independent units.

2.4. Electric Output Performance and Practical Application

Wind in nature is often random in direction and speed. F-TENG, which is designed to be surrounded by six units, can precisely determine the wind direction (the direction in which the wind
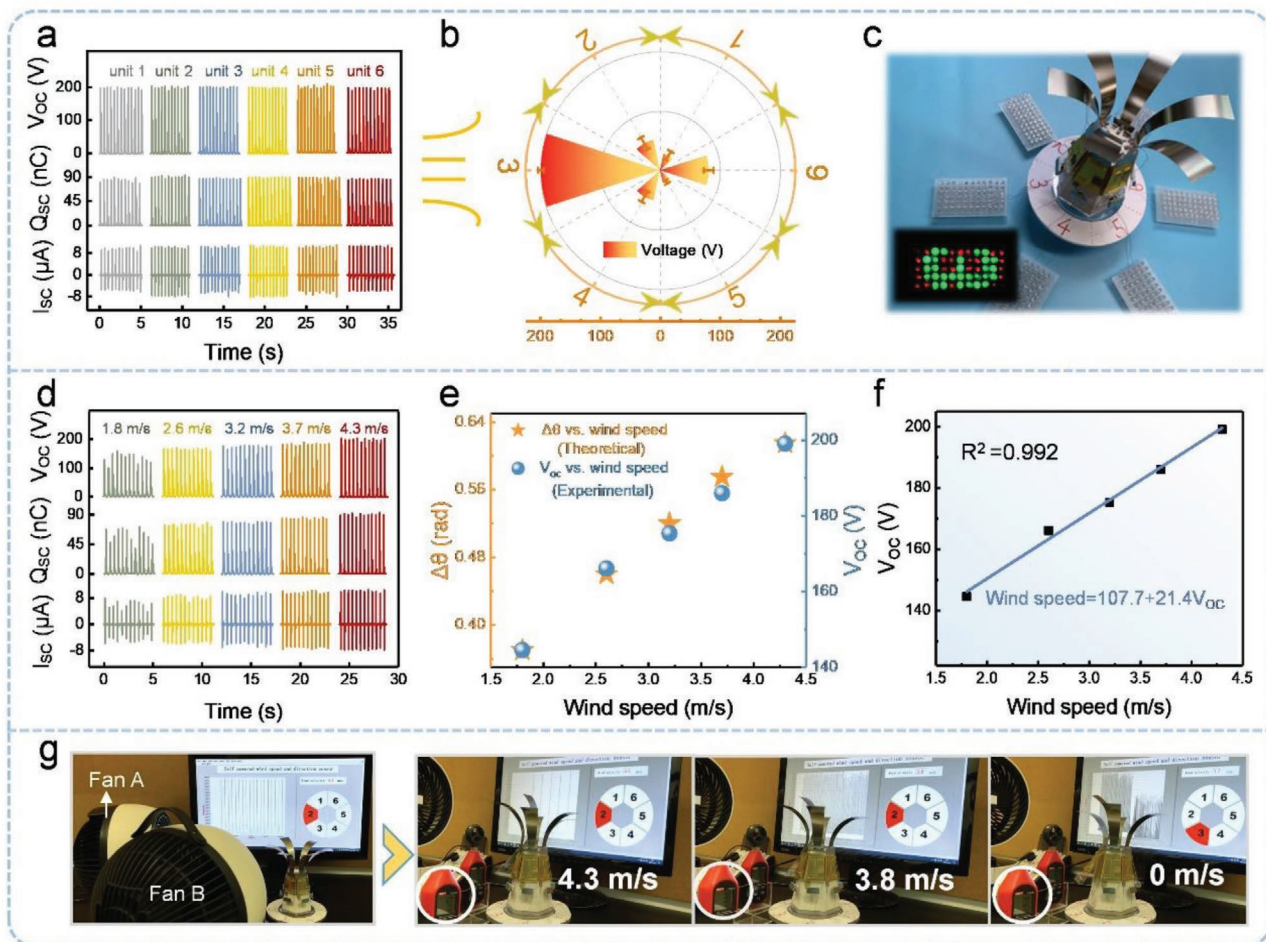
Figure 5. Self-powered wind direction and speed sensor system. a) V_{OC}, Q_{SC}, and I_{SC} of each unit when the unit is perpendicular to the wind direction at wind speed of 4.3 m s^{-1}. b) V_{OC} of six units when the wind flows in the given direction. c) A wind direction visual sensor, the inset picture shows the LEDs corresponding to the wind direction lighted by F-TENG. d) V_{OC}, Q_{SC}, and I_{SC} of a single unit for the wind speed ranging from 1.8 to 4.3 m s^{-1}. e) Comparison of $\Delta\theta$ versus wind speed in theory with V_{OC} versus wind speed in experiment. f) Linear fitting diagram of V_{OC} and wind speed. g) A self-powered wind speed and direction monitoring system based on LabVIEW software.

blows). Here, the F-TENG with a resolution of 60 is selected, and the diagram is shown in Figure 1c. In practice, the monitoring accuracy can be improved by increasing the number of units.

Based on this symmetrical design, the electrical output of each unit is basically consistent under the same conditions. The electrical signals at the wind speed of 4.3 m s^{-1} are displayed in **Figure 5**a. The V_{OC}, I_{SC}, and Q_{SC} of the single F-TENG unit are up to 199 V, 10 µA, and 90 nC, respectively. When 4.3 m s^{-1} wind blows from the calibrated direction of 3 to F-TENG, the single F-TENG unit in direction 3 shows the maximum electrical output, and the electrical signals in other directions are more than 0.5 times smaller than that in direction 3 (Figure 5b). As can be seen from the wind-impact object model, the above results are mainly because the units in other directions have very small effective contact area with the wind. So, the motion amplitude and electrical output of the units in other directions are relatively small. Based on the particularity of the device structure and output, the F-TENG is developed into a wind direction visual sensor (Figure 5c; Movie S1, Supporting Information). When the wind works on F-TENG, the

corresponding unit works and produces far more high output than the rest of the units, even at night, the flashing light to prompt the direction of the wind in time can be seen.

To further explore the specific response of F-TENG to different wind speeds, the electrical output of the single F-TENG unit, in the wind direction, was studied. As illustrated in Figure 5d, with wind speed increasing from 1.8 to 4.3 m s^{-1}, the V_{OC}, I_{SC}, and Q_{SC} all show a nearly linear upward trend. Comparing the calculation results of the theoretical model in Figure 3f with the measured V_{OC}, it was found that they were highly consistent at different wind speeds (Figure 5e). This result proves the validity and correctness of the wind-impact object model again. The relationship between the average peak value of V_{OC} and the wind speed is shown in Figure 5f. And the linear fitting curve can be described as

$$\text{Wind speed} = 107.7 + 24.1 V_{OC} \tag{35}$$

with the adjusted R^2 is greater than 0.99, which shows the high correlation between the fitting curve and the actual data. Based

**ADVANCED
SCIENCE NEWS**
www.advancedsciencenews.com

**ADVANCED
FUNCTIONAL
MATERIALS**
www.afm-journal.de

on the good linear relationship between V_{OC} and wind speed in the region where the device responds to wind speed, a self-powered wind speed and direction monitoring system based on LabVIEW platform is created, as shown in Figure 5g. The corresponding simplified logic diagrams are drawn in Figure S5, Supporting Information. Here, multiple channels are used to collect the signals of six units in the F-TENG independently, and each unit corresponds to the calibrated direction. First, the V_{OC} signals collected by the six channels are compared to obtain the direction of the wind specified by the unit with the largest output. Then the peak value of voltage is put into Equation (35), so the wind speed can be obtained. Figure 5g and Movie S2, Supporting Information show the determination of wind direction and speed for the example of directions 2 and

3, keeping the anemometer in direction 2. The above results prove that F-TENG can be used as an intelligent visual wind sensing system by LabVIEW software and LED respectively.

To evaluate the optimal matching impedance and maximum output power of F-TENG, a series of different load resistances are used to test its output performance, with a wind speed of 4.3 m s^{-1}. As illustrated in **Figure 6**a, when the resistance is small, the current is in a horizontal trend, here the formula of $P = \frac{I^2 R}{s}$ is used to calculate the output power density, where s is the contact area of two friction layers. With the increasing of external load resistance, the current gradually decreases, and the output power density presents a trend of first rising and then falling. With a load resistance of 50 MΩ, a maximum
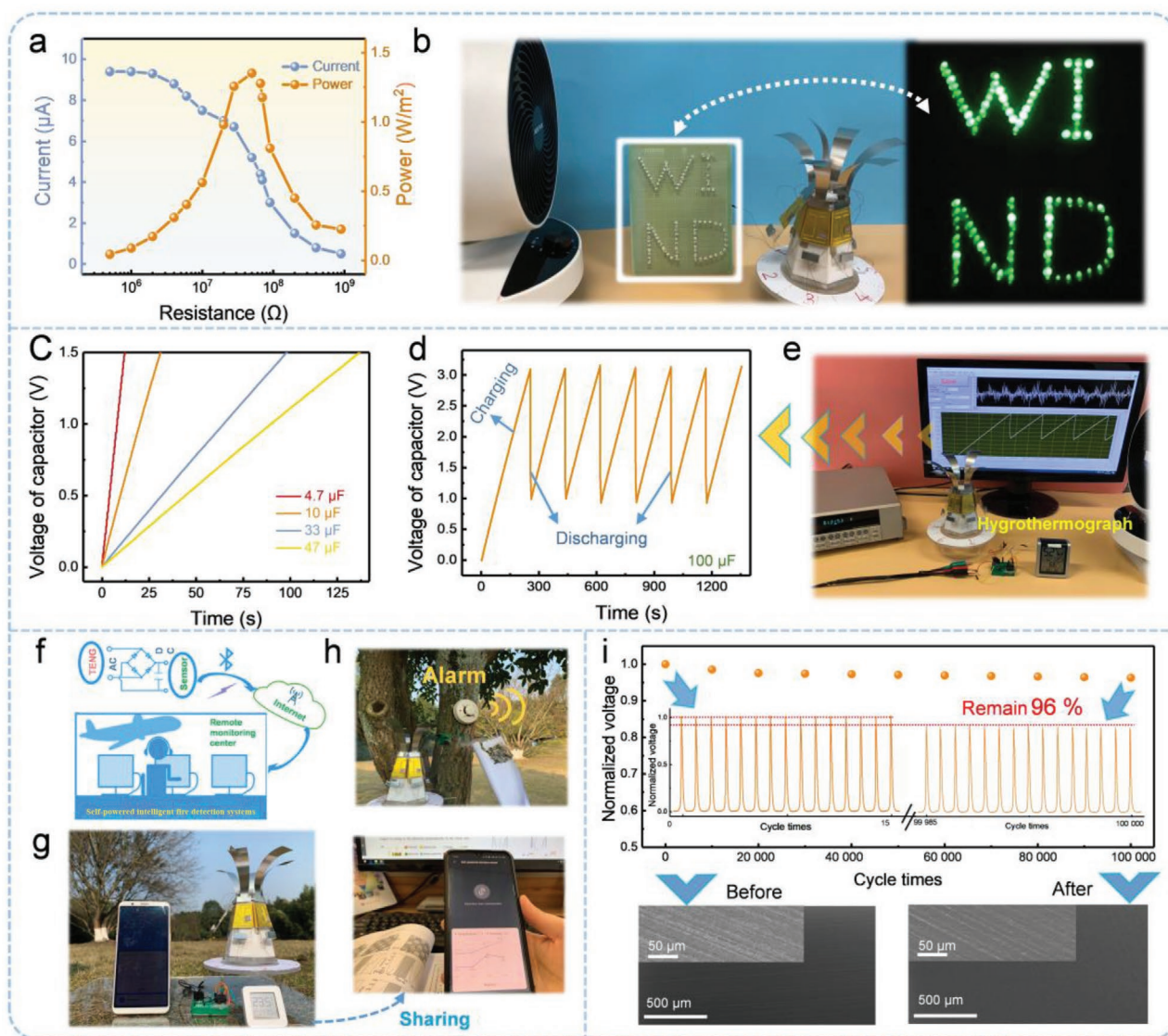
Figure 6. Applications demonstration of F-TENG as power supply. a) Output power density of the F-TENG with different load resistances. b) Directly powering 100 LEDs by the device. c) Voltage curves of the capacitors charged by the F-TENG. The d) voltage curves of the storage capacitor and e) photograph for F-TENG powering a hygrothermograph. f) Framework for the self-powered intelligent fire detection systems. g) Photographs of remote sharing of temperature and humidity information displayed on the mobile phone screen based on Bluetooth and Internet technology. h) Demonstrations for collecting wind energy as the power source of fire detector. i) Robustness test of F-TENG.

**ADVANCED
SCIENCE NEWS**

www.advancedsciencenews.com

**ADVANCED
FUNCTIONAL
MATERIALS**

www.afm-journal.de

output power density of 1.35 W m^{-2} is obtained. In addition, the device has enough energy to light up 100 LEDs, which is recorded in Figure 6b and Movie S3, Supporting Information. Moreover, different capacitors various from 4.7 to 47 µF could be charged by this device and a 4.7 µF capacitor was charged to 1.5 V within 12 s (Figure 6c). Furthermore, F-TENG was applied to drive the hygrothermograph with a 100 µF capacitor at 4.3 m s^{-1} wind speed. As shown in Figure 6d, when the capacitor voltage was charged to 3.0 V, it started to supply power to the hygrothermograph. The corresponding photo and video are shown in Figure 6e and Movie S4, Supporting Information, respectively.

Remote monitoring can realize real-time collection and rapid centralization of the field monitoring data,[35] thereby reducing the occupancy of personnel and overcoming the limitation of long-term monitoring caused by the limited energy of people. The concept diagram, using the F-TENG to collect wind energy and then supply power to the sensor, finally uploading those data to the monitoring center, is proposed in Figure 6f.

Using Bluetooth wireless technology, mobile devices for the indoor and outdoor temperature and humidity monitoring can become a reality, and further expand the scope of information sharing through the Internet (Figure 6g). Furthermore, a fire detection system based on smoke concentration is also powered by the F-TENG by using a rectifier bridge and a capacitor (Figure 6h).

Based on the above applications, an SIFDS can be constructed. On the one hand, the system can respond to the fire timely. Moreover, it can also be used for monitoring the environmental information of wind direction, wind speed, temperature, and humidity. Based on these data, the fire spread speed and direction, and even the risk of fire can be predicted.

In addition, based on the energy harvesting characteristics of F-TENG, the device can also be used in other smart fields to improve the quality of life. For example, combined with electrochromic device, a self-powered smart car window system can be built. Here, the demonstration of wind-driven smart windows based on F-TENG is displayed in Figure S6, Supporting Information.

In the process of practical application, durability is a factor that cannot be ignored. Here, at 4.3 m s^{-1} wind speed, the normalized V_{OC} of F-TENG attenuates by only 4% after 100 000 cycles, which demonstrates that the equipment has excellent fatigue endurance and reliability, as shown in Figure 6i. As an electret material, PTFE largely determines the output capacity of the device. Scanning electron microscope images in the insets of Figure 6i reveal the morphology of PTFE before and after the durability test, which indicates that the surface of the PTFE film has no obvious signs of wear and even becomes smoother. Besides, the continuous cycle tests also prove that the device has high durability, under different temperatures, humidity, and high wind speed (Figure S7, Supporting Information). The super-durable superiority assists the F-TENG to be an outstanding candidate for wind energy collection.

3. Conclusion

In summary, an F-TENG based on FIV to scavenge and monitor multidirectional breeze has been developed, and its

dynamic model (wind-impact object model) of mechanical energy and electrical energy conversion was proposed to study the interaction between solid (device) and gaseous fluid (wind). According to this model, various structural parameters and external factors are studied from theory and experiment in depth to find out the optimal structural parameters and output performance, the peak power density of a single TENG unit can reach 1.35 W m^{-2}. The practical application capabilities of F-TENG include self-powered intelligent visual wind sensing system, power for commercial capacitors, and driving hygrothermograph and fire detector were demonstrated. Those environmental monitors can provide the data basis for SIFDS to reduce the threat to public safety and social development from fire. This work provides a feasible scheme for the construction of the SIFDS based on the TENG wind energy collectors.

4. Experimental Section

Fabrication of the F-TENG: The hollow six frustums of a pyramid made of polylactic acid was fabricated by a 3D printer. The radius of the bottom and the top on the frustum of a pyramid were 5 and 3 cm respectively, and the spacing between the bottom and the top was 10 cm. The steel sheet in thickness of 0.1 mm was cut into the shape of an inverted trapezoid (24 mm × 12 mm × 97 mm) acted as the arc part. The radius of the arc part was made by extruding the steel sheet and a 3D-printed formwork with a fixed radius of curvature. The acrylic, PTFE, and Al were applied to make the contact-separation mode TENG based on the fabrication process and parameters shown in Figure S1a, Supporting Information, here, the larger acrylic served as the inclined plate part. The arc part was sticked with the inclined plate part to combine a rotatable trigger. The six rotatable triggers were fixed to the top of the frustum of a pyramid with bearings. Six pairs of mutually repulsive magnets were mounted on the lower edge of the inclined plate and the acrylic inside the frustum of a pyramid. Based on the above fabrication, a contact-separation mode TENG based on the flow-induced vibration effect was completed.

Characterization of the F-TENG: The velocity distribution of F-TENG was simulated by ANSYS software. The airflow was simulated by an electric fan. The wind speed was measured by a commercial anemometer. The extrusion force was measured by a commercial dynamometer. The Keithley 6514 system electrometer was applied to measure the electric output of F-TENG.

Supporting Information

Supporting Information is available from the Wiley Online Library or from the author.

Conflict of Interest

The authors declare no conflict of interest.

Data Availability Statement

The data that support the findings of this study are available from the corresponding author upon reasonable request.

[1] a) H. Xu, Y. Li, N. J. Huang, Z. R. Yu, P. H. Wang, Z. H. Zhang, Q. Q. Xia, L. X. Gong, S. N. Li, L. Zhao, G. D. Zhang, L. C. Tang, *J. Hazard. Mater.* **2019**, *363*, 286; b) T. Fu, X. Zhao, L. Chen, W.-S. Wu, Q. Zhao, X.-L. Wang, D.-M. Guo, Y.-Z. Wang, *Adv. Funct. Mater.* **2019**, *29*, 1806586.

[2] World Fire Statistics, https://www.ctif.org/news/world-fire-statistics-issue-no-24-2019 (accessed: April 2019).

[3] a) M. Stula, D. Krstinic, L. Seric, *Inf. Syst. Front.* **2011**, *14*, 725; b) J.-S. Chou, M.-Y. Cheng, Y.-M. Hsieh, I. T. Yang, H.-T. Hsu, *Autom. Constr.* **2019**, *99*, 1; c) M. F. Othman, K. Shazali, *Proc. Eng.* **2012**, *41*, 1204.

[4] L. Ma, R. Wu, S. Liu, A. Patil, H. Gong, J. Yi, F. Sheng, Y. Zhang, J. Wang, J. Wang, W. Guo, Z. L. Wang, *Adv. Mater.* **2020**, *32*, 2003897.

[5] H. Xie, X. Lai, H. Li, J. Gao, X. Zeng, X. Huang, X. Lin, *Chem. Eng. J.* **2019**, *369*, 8.

[6] a) S. Wang, L. Lin, Z. L. Wang, *Nano Lett.* **2012**, *12*, 6339; b) F.-R. Fan, Z.-Q. Tian, Z. L. Wang, *Nano Energy* **2012**, *1*, 328; c) T. Jin, Z. Sun, L. Li, Q. Zhang, M. Zhu, Z. Zhang, G. Yuan, T. Chen, Y. Tian, X. Hou, C. Lee, *Nat. Commun.* **2020**, *11*, 5381.

[7] a) Y. Wang, J. Wang, X. Xiao, S. Wang, P. T. Kien, J. Dong, J. Mi, X. Pan, H. Wang, M. Xu, *Nano Energy* **2020**, *73*, 104736; b) D. Liu, B. Chen, J. An, C. Li, G. Liu, J. Shao, W. Tang, C. Zhang, Z. L. Wang, *Nano Energy* **2020**, *73*, 104819; c) X. Liang, T. Jiang, Y. Feng, P. Lu, J. An, Z. L. Wang, *Adv. Energy Mater.* **2020**, *10*, 2002123; d) R. Lei, Y. Shi, Y. Ding, J. Nie, S. Li, F. Wang, H. Zhai, X. Chen, Z. L. Wang, *Energy Environ. Sci.* **2020**, *13*, 2178; e) X. Zhang, J. Hu, Q. Zeng, H. Yang, W. He, Q. Li, X. Li, H. Yang, C. Hu, Y. Xi, *Adv. Mater. Technol.* **2021**, *6*, 2001199.

[8] a) C. Zhang, Y. Liu, B. Zhang, O. Yang, W. Yuan, L. He, X. Wei, J. Wang, Z. L. Wang, *ACS Energy Lett.* **2021**, *6*, 1490; b) W. Yang, P. J. Tavner, C. J. Crabtree, Y. Feng, Y. Qiu, *Wind Energy* **2014**, *17*, 673.

[9] Z. Wang, J. An, J. Nie, J. Luo, J. Shao, T. Jiang, B. Chen, W. Tang, Z. L. Wang, *Adv. Mater.* **2020**, *32*, 2001466.

[10] Z. Wang, W. Liu, W. He, H. Guo, L. Long, Y. Xi, X. Wang, A. Liu, C. Hu, *Joule* **2021**, *5*, 441.

[11] S.-F. Leung, H.-C. Fu, M. Zhang, A. H. Hassan, T. Jiang, K. N. Salama, Z. L. Wang, J.-H. He, *Energy Environ. Sci.* **2020**, *13*, 1300.

[12] L. Yang, G. Li, Z. Zhang, X. Ma, Y. Zhao, *IEEE Trans. Sustain. Energy* **2021**, *12*, 211.

[13] Q. Zeng, Y. Wu, Q. Tang, W. Liu, J. Wu, Y. Zhang, G. Yin, H. Yang, S. Yuan, D. Tan, C. Hu, X. Wang, *Nano Energy* **2020**, *70*, 104524.

[14] S. Wang, X. Mu, X. Wang, A. Y. Gu, Z. L. Wang, Y. Yang, *ACS Nano* **2015**, *9*, 9554.

[15] a) Y. Su, G. Xie, T. Xie, H. Zhang, Z. Ye, Q. Jing, H. Tai, X. Du, Y. Jiang, *J. Phys. D: Appl. Phys.* **2016**, *49*, 215601; b) R. D. Blevins, *Prog. Nucl. Energy* **1979**, *4*, 25.

[16] H. Kim, Q. Zhou, D. Kim, I.-K. Oh, *Nano Energy* **2020**, *68*, 104379.

[17] P. Chen, J. An, S. Shu, R. Cheng, J. Nie, T. Jiang, Z. L. Wang, *Adv. Energy Mater.* **2021**, *11*, 2003066.

[18] Z. Ren, Z. Wang, Z. Liu, L. Wang, H. Guo, L. Li, S. Li, X. Chen, W. Tang, Z. L. Wang, *Adv. Energy Mater.* **2020**, *10*, 2001770.

[19] Y. Wang, E. Yang, T. Chen, J. Wang, Z. Hu, J. Mi, X. Pan, M. Xu, *Nano Energy* **2020**, *78*, 105279.

[20] J. Hu, X. Pu, H. Yang, Q. Zeng, Q. Tang, D. Zhang, C. Hu, Y. Xi, *Nano Res.* **2019**, *12*, 3018.

[21] a) J. Wang, L. Geng, L. Ding, H. Zhu, D. Yurchenko, *Appl. Energy* **2020**, *267*, 114902; b) Q. Zhu, X. Qiu, P. Coleman, I. Burnett, *J. Acoust. Soc. Am.* **2020**, *147*, 161.

[22] a) Z. L. Wang, A. C. Wang, *Mater. Today* **2019**, *30*, 34; b) H.-R. Lim, H. S. Kim, R. Qazi, Y.-T. Kwon, J.-W. Jeong, W.-H. Yeo, *Adv. Mater.* **2020**, *32*, 1901924.

[23] Z. Zhou, X. Li, Y. Wu, H. Zhang, Z. Lin, K. Meng, Z. Lin, Q. He, C. Sun, J. Yang, Z. L. Wang, *Nano Energy* **2018**, *53*, 501.

[24] Y. Yang, G. Zhu, H. Zhang, J. Chen, X. Zhong, Z.-H. Lin, Y. Su, P. Bai, X. Wen, Z. L. Wang, *ACS Nano* **2013**, *7*, 9461.

[25] Y. C. Lai, Y. C. Hsiao, H. M. Wu, Z. L. Wang, *Adv. Sci.* **2019**, *6*, 1801883.

[26] L. Xu, L. Xu, J. Luo, Y. Yan, B. E. Jia, X. Yang, Y. Gao, Z. L. Wang, *Adv. Energy Mater.* **2020**, *10*, 2001669.

[27] K. Han, J. Luo, Y. Feng, Q. Lai, Y. Bai, W. Tang, Z. L. Wang, *ACS Nano* **2020**, *14*, 2751.

[28] Y. Zhang, Q. Zeng, Y. Wu, J. Wu, S. Yuan, D. Tan, C. Hu, X. Wang, *Nano-Micro Lett.* **2020**, *12*, 175.

[29] a) R. K. Brahma, I. Padhy, B. Pradhan, *Warme Stoffubertrag* **1990**, *26*, 41; b) H. M. Hofmann, M. Kind, H. Martin, *Int. J. Heat Mass Transfer* **2007**, *50*, 3957; c) E. Fuchs, H. Köhler, J. P. Majschak, *Chem. Ing. Tech.* **2019**, *91*, 455.

[30] a) S. Beltaos, N. Rajaratnam, *J. Hydraul. Res.* **2010**, *15*, 311; b) P. Weber, J. Hureau, *Eur. J. Mech. B Fluids* **1999**, *18*, 283.

[31] a) G. Cafiero, C. S. Greco, T. Astarita, S. Discetti, *Exp. Therm. Fluid Sci.* **2016**, *78*, 334; b) A. Mishra, H. Yadav, L. Djenidi, A. Agrawal, *Exp. Fluids* **2020**, *61*, 1; c) X. K. Wang, G. P. Niu, S. Q. Yuan, J. X. Zheng, S. K. Tan, *Fluid Dyn. Res.* **2015**, 47, 025501.

[32] P. Cornille, *Prog. Energy Combust. Sci.* **1999**, *25*, 161.

[33] H. Yang, M. Deng, Q. Zeng, X. Zhang, J. Hu, Q. Tang, H. Yang, C. Hu, Y. Xi, Z. L. Wang, *ACS Nano* **2020**, *14*, 3328.

[34] Y. Yang, *IOP Conf. Ser.: Mater. Sci. Eng.* **2019**, *563*, 032048.

[35] Z. Lv, B. Hu, H. Lv, *IEEE Trans. Industr. Inform.* **2020**, *16*, 1957.